





Femtosecond laser direct nanolithography of perovskite hydration for temporally programmable holograms

Received: 31 March 2024

Yinan Zhang ^{1,2,3} ✉, Shengting Zhu^{1,2,3}, Jinming Hu ^{1,2} & Min Gu ^{1,2} ✉

Accepted: 29 July 2024

Published online: 06 August 2024

 Check for updates

Modern nanofabrication technologies have propelled significant advancement of high-resolution and optically thin holograms. However, it remains a long-standing challenge to tune the complex hologram patterns at the nanoscale for temporal light field control. Here, we report femtosecond laser direct lithography of perovskites with nanoscale feature size and pixel-level temporal dynamics control for temporally programmable holograms. Specifically, under tightly focused laser irradiation, the organic molecules of layered perovskites (PEA)₂PbI₄ can be exfoliated with nanometric thickness precision and subwavelength lateral size. This creates inorganic lead halide capping nanostructures that retard perovskite hydration, enabling tunable hydration time constant. Leveraging advanced inverse design methods, temporal holograms in which multiple independent images are multiplexed with low cross talk are demonstrated. Furthermore, cascaded holograms are constructed to form temporally holographic neural networks with programmable optical inference functionality. Our work opens up new opportunities for tunable photonic devices with broad impacts on holography display and storage, high-dimensional optical encryption and artificial intelligence.

Holograms, as an approach to reconstructing the amplitude and phase information of 3D objects, have been used to control the diffractive light field in many applications, such as display and storage^{1,2}, encryption³, optical trapping⁴, artificial neural networks⁵, and all-optical machine learning⁶. With the rapid development of modern nanofabrication technologies, such as electron beam lithography (EBL), metasurface holograms, made of subwavelength metallic or dielectric elements, have been demonstrated to achieve high resolution, low noise, and high efficiency reconstructed images in the microwave, terahertz, infrared, and visible spectral range^{7–10}. Now, significant efforts are being devoted to translating these static holograms to dynamic holograms^{11–16} for light field control in the time domain. In the microwave frequency, digit coding metasurfaces made of electric diode-controlled metallic structure enable individual pixel reconfigurability and real-time, multiple arbitrary holography¹¹.

While in the visible range, it remains a significant challenge to tune the complex hologram patterns at the nanoscale. Recent demonstration of visible dynamic holograms through mechanical stretching¹², thermal-induced phase-change¹³, and nanostructure swelling¹⁴ is difficult to impart the individual pixel different time-varying properties and only achieved holographic image switching. Although chemically active plasmonic metasurfaces show the potential of pixel-level temporal dynamics control¹⁵, they require complex and multiple EBL and lift-off steps to create nanostructures with different chemical compositions and bulky external control apparatus.

In contrast, laser printing is a contactless, one-step patterning technology with high resolution and 3D capabilities^{17–20} and has been used to fabricate holograms through the subwavelength photo-reduction of graphene oxide²¹, ablation of ultrathin topological thin films and atomically thin noble metal dichalcogenides^{22,23} and writing

¹School of Artificial Intelligence Science and Technology, University of Shanghai for Science and Technology, Shanghai, China. ²Institute of Photonic Chips, University of Shanghai for Science and Technology, Shanghai, China. ³These authors contributed equally: Yinan Zhang, Shengting Zhu.

✉ e-mail: zhangyinan@usst.edu.cn; gumin@usst.edu.cn

of 3D nano-resolution lithium niobate crystals²⁴. Particularly, 4D laser printing fabricates nanoscale shape memory polymer structures with time-varying shapes, properties, and functionalities²⁵, endowing the fabricated holograms reconfigurable under external heating stimuli²⁶. However, the function tunability is rather limited with a simple on/off switch and the hologram patterns are limited to a single-layer framework. To fully explore temporally holographic light field control, it is highly desired to develop new printing materials and mechanisms with pixel-level temporal dynamics control and multilayer framework.

Lead halide perovskites, as the most attractive semiconductor materials in the past decade in the photovoltaic (PV) community^{27,28}, are rapidly emerging in the field of nanophotonics with various demonstrated functional devices, including on-chip vortex microlasers²⁹, meta-holograms³⁰, optical data storage and three-dimensional (3D) display^{31,32}, nonlinear optical encoding devices³³, and structural color systems³⁴. Due to their low formation energy, perovskites usually exhibit instability against moisture, oxygen, photoexcitation, and thermal heating which is commonly regarded to adversely affect device performance. Specifically, under a humid atmosphere, perovskites experience hydration, a phenomenon of moisture-induced changes in the chemical structure and corresponding optical properties³⁵. However, from a different perspective, this lability represents a potential stimuli-responsive material platform for constructing time-varying photonic devices. We hypothesized that the surface of perovskites could be locally modified to control the hydration rate and hence the variation in optical properties with time. Particularly, the recently demonstrated three-dimensional direct laser lithography of perovskites with tunable chemical composition offers a potentially viable method³².

In this work, we report femtosecond (fs) laser direct lithography of perovskites with nanoscale feature size and pixel-level temporal dynamics control for temporally programmable holographic light field

control. This is achieved by means of two-photon absorption-induced localized hydration control. We discover that under tightly focused fs laser irradiation, the layered (PEA)₂PbI₄ perovskites undergo localized structural and compositional changes due to the exfoliation of the organic molecules from the materials (Fig. 1a). This creates material thickness reduction with nanometric precision accompanying with subwavelength inorganic PbI₂ layers on the surface that act as a local capping layer, retarding the hydration of the perovskite. Therefore, the hydration time constant, defined as the duration required for transmission at the exciton absorption wavelength to approach 100%, and the initial transmission state can be elaborately manipulated by adjusting the laser fluence (Fig. 1b). Leveraging this nanoscale pixel-level temporal dynamics control and the developed advanced inverse design methods, we demonstrate temporally programmable holograms in which multiple independent images are multiplexed with low cross talk (Fig. 1c). Furthermore, cascaded holograms are constructed to form a temporally holographic neural network with programmable optical inference functionality. This study exceeds the current lithography of tunable photonic devices by achieving sub-diffraction feature size, pixel-level temporal dynamics control, and temporally programmable functionality with simple and fast one-step laser printing, opening up new opportunities for tunable nanophotonics in the time domain.

Results

To investigate the feasibility of temporal lithography of perovskites, we first studied their local modulation and corresponding hydration control. (PEA)₂PbI₄ perovskite thin films are synthesized and fabricated on clean glass substrates following the methods in the literature³⁶. (PEA)₂PbI₄ are layered Ruddlesden–Popper perovskites consisting of inorganic layers of metal-halide perovskites confined by

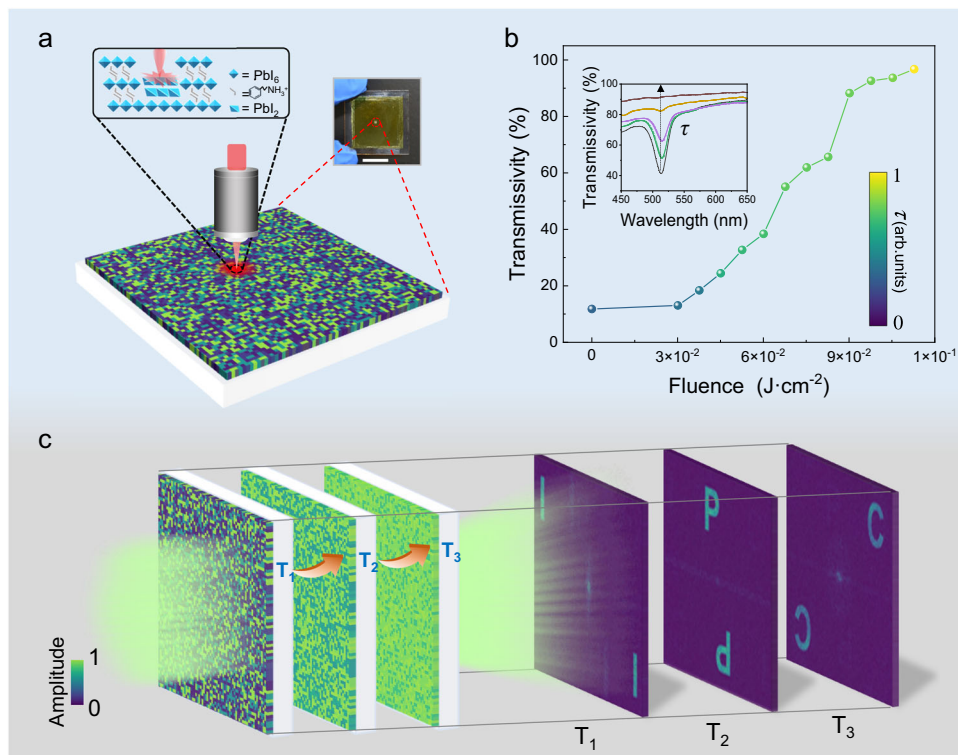


Fig. 1 | Femtosecond laser nanolithography of perovskite hydration for temporally programmable holograms. **a** Schematic of the laser patterning of (PEA)₂PbI₄ perovskite hologram and a photo of the fabricated sample. Scale bar, 1 mm. The zoom-in at the focal spot shows the schematic of the local change of the perovskites. **b** Perovskite transmission and hydration time constant control by the

laser fluence. The inset figure shows perovskites' transmission spectra evolution with a pronounced dip at 515 nm, corresponding to the exciton absorption peak. τ is the time constant defined as the duration required for the transmission dip to approach 100%. **c** Schematic diagram of the fabricated perovskite holograms for temporally programmable holographic images.

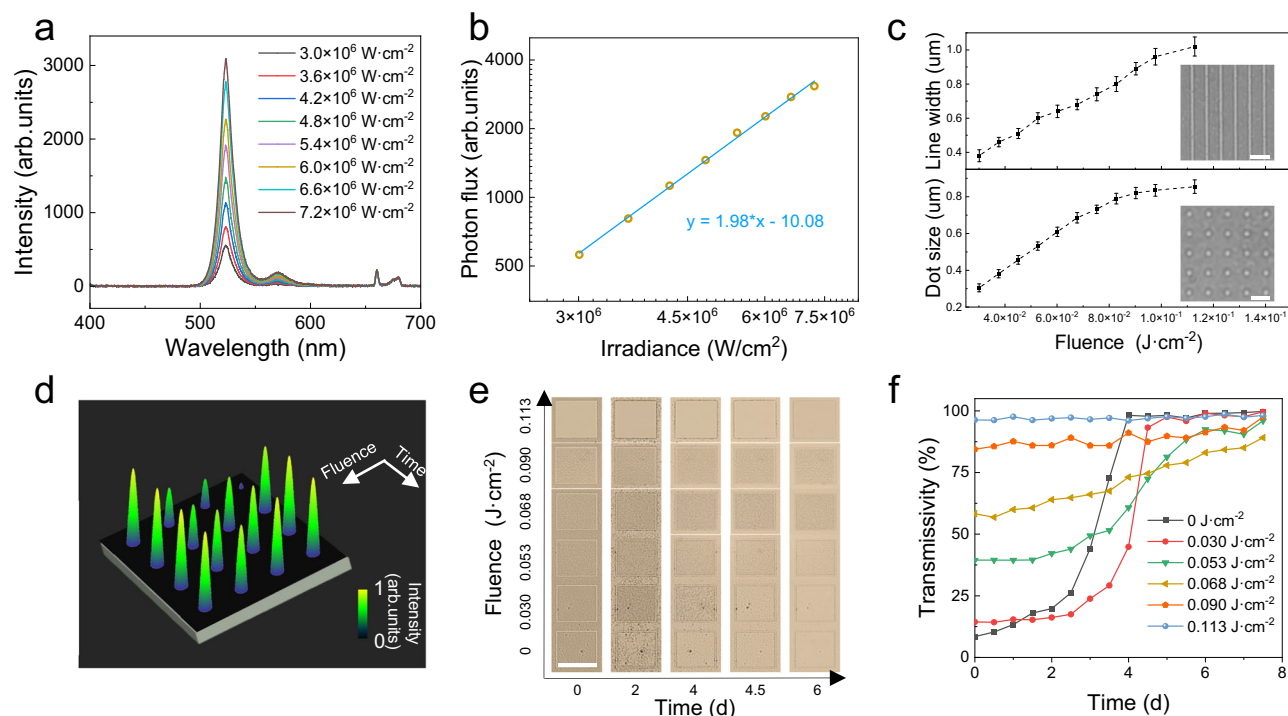


Fig. 2 | Nanoscale perovskite lithography and temporal dynamics control. **a** The fluorescence spectra of the $(\text{PEA})_2\text{PbI}_4$ perovskite thin films under the fs laser excitation. **b** The double logarithm plots of the fluorescence intensity vs. laser power density with a linear fit. **c** The printed line width and dot size as a function of the laser fluence, with the insets showing representative SEM images of the line and dot arrays. Scale bars, $3\ \mu\text{m}$. Error bars (standard deviation) were calculated by

randomly selecting five different points (lines) and the data were expressed as mean values \pm SD. **d** The transmission signal evolution of the microscopy images of four printed dots with various laser fluences. **e** Optical microscopy image evolution of the laser-processed square-shaped perovskite areas. Scale bar, $50\ \mu\text{m}$. **f** Transmission change at the wavelength of $515\ \text{nm}$ of the perovskite thin film after laser processing with different fluences.

wide-bandgap and low-dielectric-constant organic cations^{37,38}. The observed X-ray diffraction (XRD) patterns corresponding to the crystal planes of $(\text{PEA})_2\text{PbI}_4$ and the atomic force microscopy (AFM)/scanning electron microscopy (SEM) images (Supplementary Fig. 1a–c) indicate that $(\text{PEA})_2\text{PbI}_4$ thin films have been prepared well, with high uniformity and smoothness. Owing to the quantum and dielectric confinement effect, the materials show a narrow and intense exciton absorption peak at $515\ \text{nm}$ under room temperature (Supplementary Fig. 1d); thus, we choose to target this absorption effect for light transmission modulation to realize amplitude holograms in our work. Notably, phase modulation can also be achieved by optimizing the material thickness and laser writing recipe. The thickness and the initial transmission at the wavelength of $515\ \text{nm}$ can be controlled by the spin-coating process (Supplementary Fig. 2). In our experiment, $\sim 160\ \text{nm}$ thick $(\text{PEA})_2\text{PbI}_4$ thin films are produced with a spin-coating speed of $2000\ \text{rpm}$, corresponding to an initial light transmission of $\sim 10\%$, sufficiently low enough for multilevel amplitude modulation.

In the laser lithography process, a fs laser with a wavelength of $800\ \text{nm}$ is tightly focused on the surface of the perovskite thin films with a high NA ($0.65\times$) objective lens. Because $(\text{PEA})_2\text{PbI}_4$ thin films are transparent at the wavelength of $800\ \text{nm}$ and their third-order nonlinear susceptibility is rather large, we expect multiphoton absorption in the lithography process. Indeed, two-photon absorption is experimentally confirmed by the linear slope of the double logarithm plot of the fluorescence intensity vs. laser power density (Fig. 2a, b). To investigate the influence of the laser fluence on the feature size, the laser-printed line width and dot size as a function of the laser fluence were measured and plotted in Fig. 2c, with the insets showing representative SEM images of the line and dot arrays. The minimum line width and dot size can be controlled to be as small as ~ 400 and $\sim 300\ \text{nm}$, which are smaller than the optical diffraction limit ($\sim 750\ \text{nm}$) for the 0.65 NA objective lens and $800\ \text{nm}$ laser wavelength.

Such ultrahigh-resolution laser processing stems from the observed nonlinear two-photon absorption and the ultralow thermal conductivity ($0.1\text{--}0.2\ \text{W m}^{-1}\ \text{K}^{-1}$) of layered perovskites³⁹, which can confine the local heating in the focal spot region during the ultrashort laser pulse irradiation. In addition, the laser wavelength, energy density control as well as the NA of the objective lens contribute to the nanoscale feature size.

Next, we investigate the changes in the local optical transmission over time with various laser fluences. The microscopic image of the printed dot array with various laser fluences is acquired during the hydration process in the ambient air ($25\ ^\circ\text{C}$, $\sim 30\%$ humidity). The transmission signal of the printed dots as a function of time with various laser fluences is plotted in Fig. 2d. Clearly, the dot with lower laser fluence hydrates faster than that by higher laser fluence, indicating the feasibility of controlling the temporal dynamics at the nanoscale by our methods. To accurately quantify this, we fabricated a few square-shaped ($50 \times 50\ \mu\text{m}$) perovskite patterns with different laser fluences and measured their local transmission over time. Their initial transmission spectra are firstly measured, demonstrating near-continuously spectra elevation, with a pronounced increase at a wavelength of $515\ \text{nm}$ (Supplementary Fig. 3). This enables a multilevel amplitude modulated hologram with decent diffraction efficiency (Supplementary Fig. 4). The optical microscopy images and transmission spectra of the laser-processed perovskites are recorded during the hydration process. The laser-processed area undergoes a hydration process, as evidenced by a change in the appearance of the surface of the sample under optical microscopy (Fig. 2e) and an upward shift of the overall transmission spectra over time (inset of Fig. 1b). The change in transmission at the wavelength of $515\ \text{nm}$ after laser processing is also analyzed. Unambiguously, the unprocessed area undergoes fast hydration, with its transmission approaching 100% within 4 days (Fig. 2f). In contrast, the processed areas show a relatively slow

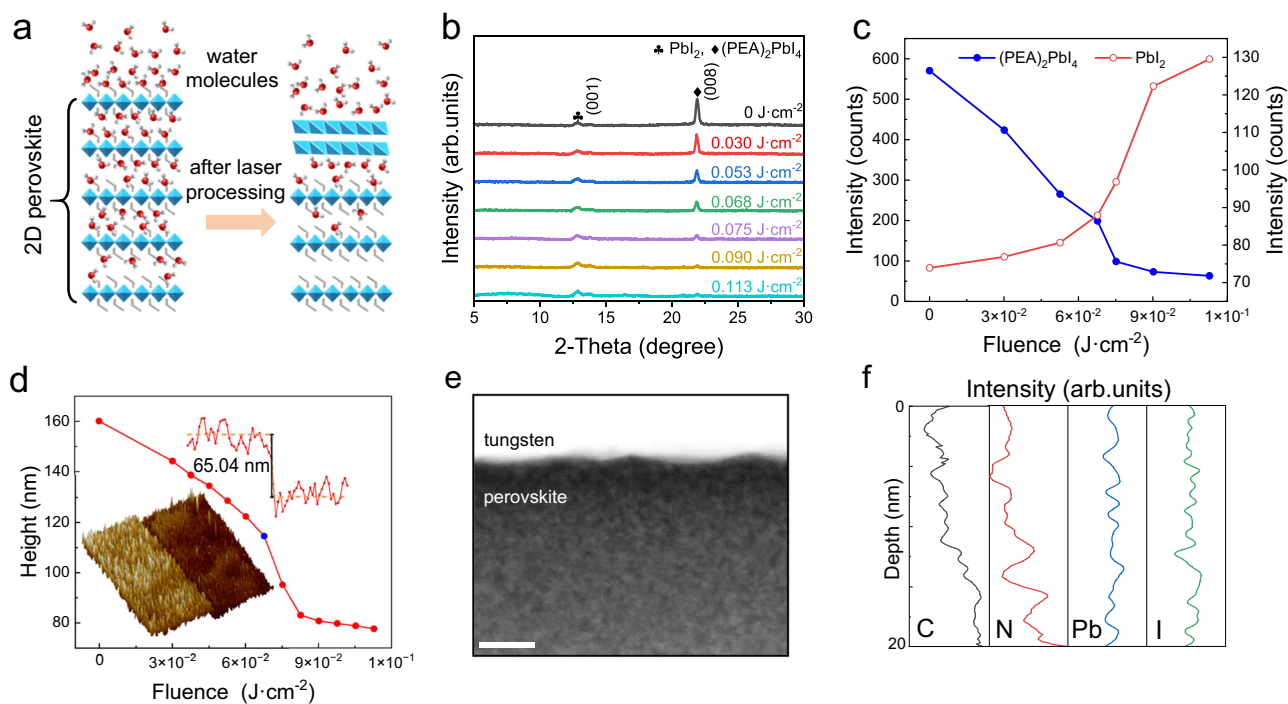


Fig. 3 | Mechanism of the localized hydration control. **a** Schematic mechanism of the laser-induced perovskite hydration retardation. The surface PbI_2 layer slows down the water molecules penetrating the perovskites. **b** X-ray diffraction (XRD) patterns of the layered perovskites processed with various laser fluences. **c** Intensities of the XRD characteristic peaks of $(\text{PEA})_2\text{PbI}_4$ and PbI_2 with various

laser fluences. **d** Height changes of the perovskite thin film after laser processing with one example of $50 \times 50 \mu\text{m}$ atomic force microscopy (AFM) images. **e** Cross-sectional transmission electron microscopy (TEM) image of the perovskite thin film after laser processing. Scale bar, 10 nm. **f** The chemical element distribution along the cross-sectional TEM image.

hydration process, leading to a smooth transmission increase. The hydration time constant of the area processed by 0.030 $\text{J}\cdot\text{cm}^{-2}$ and 0.053 $\text{J}\cdot\text{cm}^{-2}$ laser fluence are 4.5 days and 7.5 days, respectively. The higher the laser fluence is, the slower the transmission increases. When the laser fluence is high enough, the transmission is initially close to 100% and remains unchanged. Thus, the local optical transmission and how it changes over time can be controlled by the laser fluence. This is also confirmed by measurements of the imaginary part of the refractive index and its changes of the thin films after laser processing (Supplementary Fig. 5). One important feature of the transmission change is that the transmission of the unprocessed area or the area processed with a low laser fluence surpasses that of the area processed with a high laser fluence, indicating optical state reversal. The various hydration time constants controlled by the laser fluence and the optical state reversal play key roles in designing temporally programmable holograms and holographic neural networks.

The local optical transmission change over time can be explained by the proposed model in Fig. 3a, where the hydration of the materials in the ambient air is retarded by the surface inorganic PbI_2 layer after exposure to the fs laser irradiation. To verify this surface composition change, micro-XRD patterns of square perovskite areas processed with various laser fluences are measured. Clearly, the as-prepared perovskite thin film shows a pronounced (008) lattice plane peak, and the peak intensity gradually decreases as the laser fluence increases from 0.030 to 0.113 $\text{J}\cdot\text{cm}^{-2}$ (Fig. 3b, c). In contrast, the intensity of the (001) lattice plane peak of PbI_2 increases, indicating that the organic molecules are removed and an inorganic PbI_2 layer is left behind. Furthermore, the X-ray photoelectron spectra (XPS) of the perovskites (Supplementary Fig. 6) corroborate that the surface organic–inorganic $(\text{PEA})_2\text{PbI}_4$ layer gradually changes to inorganic PbI_2 , as the amounts of C and N gradually decrease.

AFM shows that the thickness of the film decreases from ~160 to ~75 nm as the laser fluence increases (Fig. 3d). The thickness control can be <10 nm, demonstrating high precision of laser processing at the

vertical dimension. The ratio between the thin film thickness after processing by 0.113 $\text{J}\cdot\text{cm}^{-2}$ laser fluence (the highest fluence tested) and the initial thickness is ~0.46, roughly agreeing with the ratio of the lattice constants of the two phases of interest along the *c*-axis (6.78 Å for PbI_2 and 16.13 Å for $(\text{PEA})_2\text{PbI}_4$). This indicates that the organic molecules are removed under the laser processing, causing the layered structure to collapse and leading to a reduced thin film thickness. When the laser fluence is >0.083 $\text{J}\cdot\text{cm}^{-2}$, the thickness remains almost constant, indicating that the organic molecules have mostly been removed. The cross-sectional transmission electron microscopy (TEM) (Fig. 3e) and the corresponding chemical element distribution (Fig. 3f) further confirmed that the surface of the perovskite converts to inorganic PbI_2 .

Next, we aim to employ the laser-induced variation in the hydration time constant to design temporally holograms based on a superpixel scheme, in which binary amplitude holograms with different hydration time constants can be spatially multiplexed. The binary holograms are made of different low transmission pixels and high transmission (100%) pixels, corresponding to 0.113 $\text{J}\cdot\text{cm}^{-2}$ laser fluence. Before we construct the superpixel holograms, we first determine the various optical diffraction time constants by examining simple optical grating structures consisting of areas processed with lasers at various fluences and 0.113 $\text{J}\cdot\text{cm}^{-2}$. As shown in Supplementary Fig. 7, both the microscopy images of the gratings and the diffraction patterns gradually fade until they disappear. The signal-to-noise ratio, defined as the ratio between the intensity of the first-order diffraction spot and that of a nearby area, is also presented, demonstrating the various diffraction time constants.

Based on the above results, we design a holographic image of the digit 8, with its three image sections (left vertical lines, middle horizontal lines, and right vertical lines) corresponding to various time constants, with the aim of temporal holography display where the image sequentially evolves from digits 8 to 3 and 1 (Fig. 4a).

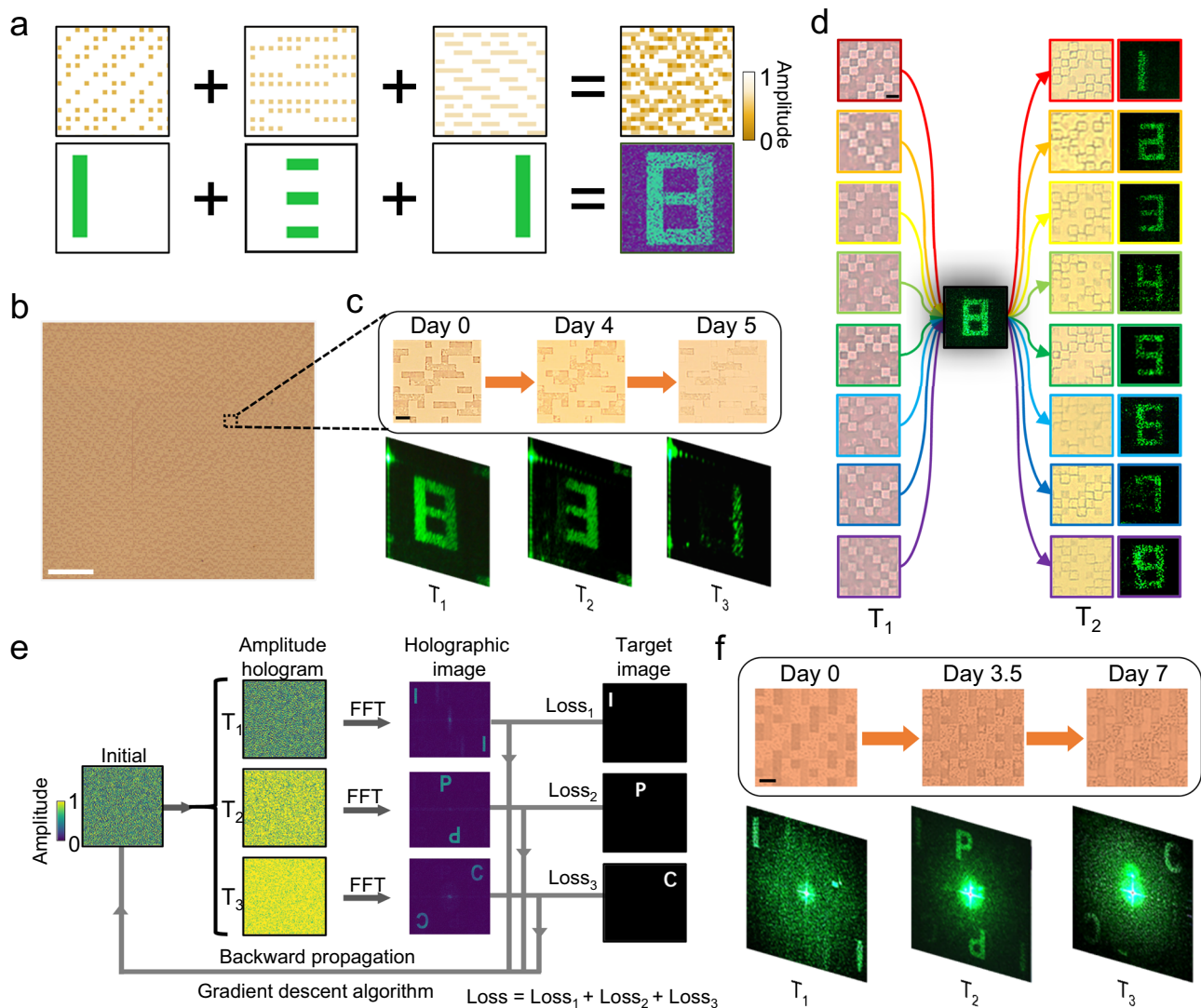


Fig. 4 | Temporally programmable holograms. **a** Illustration of designing the superpixel temporal hologram, in which binary amplitude holograms corresponding to different image parts of digit 8 can be spatially multiplexed. **b** The fabricated 180×180 superpixel hologram with a pixel size of $3 \mu\text{m}$. Scale bar, $200 \mu\text{m}$. **c** The zoom-in temporal hologram microscopy images and corresponding holography images. Scale bar, $5 \mu\text{m}$. **d** The experimental results of temporal

hologram encryption, showing that at time T_1 , all the fabricated holograms display digit 8 while at time T_2 , various digit holography images appear. Scale bar, $5 \mu\text{m}$. **e** Inverse optimization flow chart for three independent holography images I, P, and C (FFT fast Fourier transform). **f** Hologram microscopy images and corresponding experimental holography images of I, P, and C. Scale bar, $5 \mu\text{m}$.

Experimentally, a hologram with a pixel size of $3 \mu\text{m}$ and an area of $1.08 \times 1.08 \text{ mm}$ is fabricated (Fig. 4b). A relatively large pixel size is employed to better visualize the pixel change under the microscope. Magnified optical images (Fig. 4c) of the experimentally fabricated hologram clearly show the changes in the superpixels over time. Furthermore, holographic images of digit 8 composed of two different section combinations can be designed, which can be used to hide various digit information (from 1 to 9 except 8) behind digit 8 in the time domain (Supplementary Fig. 8, Fig. 4d).

Temporally dynamic holography demonstrated above enables the realization of holography multiplexing that exhibits multiple independent images in the time domain. To achieve this, we introduce advanced inverse design methods with multiobjective optimization to design such holograms, with Fig. 4e illustrating the optimization flow chart. Gradient descent algorithms using the total loss function defined as the calculated images against the target images at different times are developed to optimize the amplitude profiles, in which four states corresponding to the laser fluence of 0, 0.030, 0.053, and 0.113 J cm^{-2} are used. The optimum time points for the appearance of

the images are obtained through a global search of the time parameter. As an example, three targeted images of the letters I, P, and C (the capital initials of the Institute of Photonic Chips) are designed to be sequentially retrieved in the time domain. The optimized 300×300 pixel hologram design is shown in Supplementary Fig. 9, with its simulated images retrieved presented along with the time-changing transmission curves of the four levels of the hologram.

Impressively, the three simulated retrieved images show very low cross talk (0.83, 0.94, 0.86), which is defined as the ratio of the intensity of one image to the sum of the intensities of the three images. Even though the three holographic images are designed to be at the same location, the optimization results still show very low cross talk (0.92, 0.88, 0.91), as shown in Supplementary Fig. 10. Notably, the time point for the appearance of the second image is on the 3.5th day, at which time the transmission for the pixel without laser processing surpasses that of the pixels processed with a laser fluence of 0.030 and 0.053 J cm^{-2} . The third image appears on the 7th day, when the transmission of the pixels without laser processing and processed with a 0.030 J cm^{-2} laser surpasses that of the pixels processed with a laser

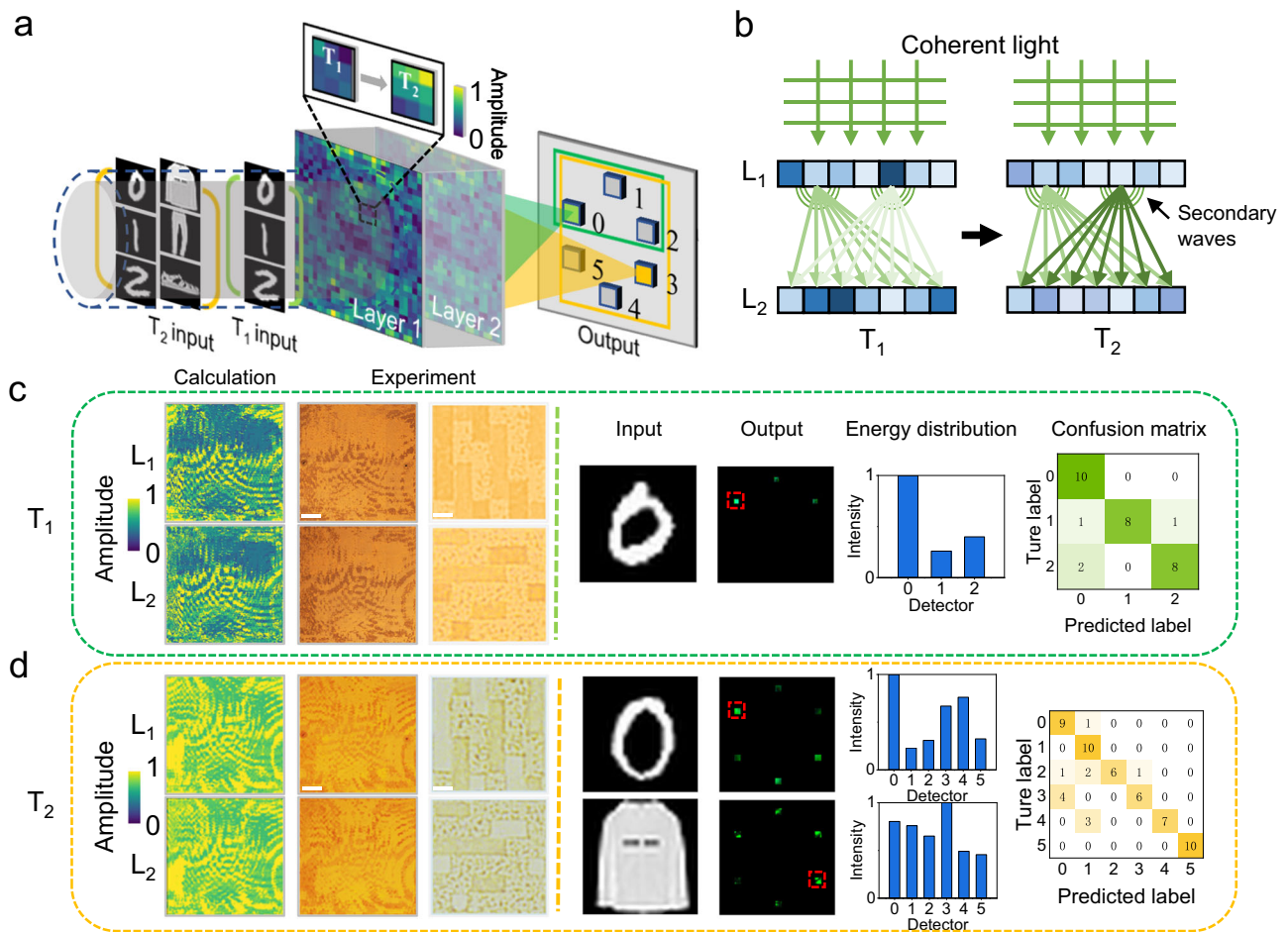


Fig. 5 | Temporally programmable holographic neural network. **a** Schematic of two-layer holographic neural network inference with sequential handwritten digit and handwritten digit + fashion product classification functionalities at times T_1 and T_2 . Detectors 0–2 correspond to digits 0–2, while detectors 3, 4, and 5 correspond to t-shirts, trousers, and shoes, respectively. **b** Schematic of the optical interconnections between the two holographic layers at times T_1 and T_2 . **c, d** The

calculated and experimental amplitude hologram profiles and corresponding classification results. Scale bars, 100 and 3 μm . Representative input images, camera images with red boxes indicating the targeted detector regions, the energy distribution percentage in the targeted regions, and the confusion matrix are presented.

fluence of 0.053J cm^{-2} . This result is reasonable because a new different holography image can potentially appear only if the relative amplitudes of the hologram pixels change.

To verify these simulation results, a 300×300 hologram with a pixel size of $3\ \mu\text{m}$, corresponding to a total size of $900 \times 900\ \mu\text{m}$, is experimentally fabricated, as shown in Supplementary Fig. 9c. Three experimentally obtained images retrieved at different time points are shown in Fig. 4f along with magnified optical images of the hologram at the corresponding times. The experimentally retrieved images also show low cross talk (0.91, 0.76, 0.79), agreeing well with the simulated results. Although the time scale for temporally holography display spans up to 1 week, it can be significantly reduced within 1 day by increasing the environmental humidity to 85% (Supplementary Fig. 11). The demonstrated temporally multiplexed independent holography images are thus far the real demonstration of temporally multiplexed hologram to the best of our knowledge. We expect that more than three temporal holography images can be achieved by using multiple holographic layers.

Holograms provide an excellent optical platform to mimic artificial neural networks in the optical domain, which shows unparalleled capabilities for executing artificial intelligence tasks with ultralow energy consumption and high computational power at the speed of light compared with their electronic counterparts^{5,6,40–44}. However, as with most holograms, these holographic neural networks are hard to

tune in the time domain once they are fabricated, limiting their widespread applications. Although a few recent attempts on dynamic holographic neural networks were demonstrated by using spatial light modulators⁴⁵ and digital metasurfaces with millimeter-scale pixel size⁴⁶, these methods rely on complicated and bulky external electrical circuit control systems to individually program the pixels. In contrast, our demonstrated fs laser lithography of perovskite hydration enables an optically programmable holographic neural network with much smaller neuron size with large computational power and temporal evolution functionality, i.e., the functionality can change with time under the hydration stimuli. As a proof-of-concept demonstration, we design holographic neural networks that change in functionality from simple digit image classification to more complicated digit and clothing product image classification with time to mimic the function evolution of the human brain, as shown in Fig. 5a. During the temporal evolution, the optical interconnections, particularly the relative connection strength between the two layers, change (Fig. 5b), leading to time-changing output optical fields.

We train the networks on amplitude profiles of the two holographic layers using the error back-propagation algorithm, which is based on the stochastic gradient descent approach (Supplementary Fig. 12; see section “Methods” for details). A total loss function corresponding to the summation of the losses at times T_1 and T_2 is used, in which the loss is defined as the total mean square error (MSE) of the

output energy distribution relative to the target image at the output plane. In the optimization, four amplitude levels, corresponding to pixels without laser processing and processed with 0.030, 0.053, and 0.113 J cm⁻² laser fluence are employed. The neuron number is 200 × 200, and the neuron size is 3 μm. The distance between the two hologram layers is set as 0.7 mm, which is the thickness of the glass slide used in the experiment, and the input and output planes are 5 cm from the hologram layers. A total of 6000 images from the Modified National Institute of Standards and Technology (MNIST) handwritten digit database and Fashion-MNIST dataset are employed to perform the training with the loss function. The numerical training results are shown in Supplementary Fig. 13, achieving decent classification accuracies of 98.6% at time T_1 (Day 0) and 89.9% at time T_2 (Day 4).

Next, we validate the temporal function change of the neural network, with the experimental results shown in Fig. 5c, d. At time T_1 , the neural network performs three-digit (0, 1, and 2) classification, with an experimental accuracy of 86.6%. The energy distributions observed at the network output plane for the test digits are also shown, clearly demonstrating that the holographic layers learn to focus the input energy of digits 0, 1, and 2 into the target region. At time T_2 , the neural network implements the task of clothing products (t-shirts, trousers, and shoes) and digit classification, with an accuracy of 80%. This result indicates that the function of the network evolves in a programmable way that conserves the function at T_1 . The very low accuracy (58%) when performing fashion product classification at time T_1 (Supplementary Fig. 14) confirms that the neural network can only execute this additional task at T_2 . By increasing the distance of the two holographic layers to a fully connected network, a higher classification accuracy and a larger number of classifications can be expected.

The demonstrated perovskite hydration nanolithography, temporally programmable holograms, and holographic neural network exceed the achievements of current tunable photonic devices, which will impact a wide range of applications, including holography optical data storage, high-dimensional optical encryption, artificial intelligence, and highly stable perovskite PVs. Particularly, with further development of the materials, temporally programmable holograms with reversibility and fast-changing rate within minutes and seconds beyond the current results can be envisaged, which will undoubtedly open new opportunities for research on tunable nanophotonics in the time domain.

Methods

Perovskite thin film fabrication

The (PEA)₂PbI₄ powder was synthesized by the following procedures³⁶. In total, 54.6 mg PbI₂ (99.999%, trace metals basis, perovskite grade) was firstly dissolved in 0.5 mL HI (57 wt% in H₂O, with hypophosphorous acid as a stabilizer, assay 99.95%). Then 1 mL CH₃OH (>99.9%) was slowly injected on top of the PbI₂/HI solution. After that, 0.03 mL 2-phenethylamine liquid was added into the CH₃OH layer to form red and laminar crystals (yield ~76% according to the PbI₂), which settled down at the bottom of the vessel overnight. At last, these crystals were rinsed with massive EtOAc and collected by vacuum filtration, followed by drying in vacuum at 50 °C for 6 h. The perovskite precursor solution was synthesized by dissolving the perovskite powders in the solvent (DMF:DMSO = 9:1) with a concentration of 100 mg/mL. Then the solution was spin-coated on cleaned glass substrates for 60 s with various rotation speed, and then the sample was annealed at 70 °C for 30 min to evaporate the residual solvent. All fabrication processes were finished in an Ar-filled glovebox.

Temporally programmable hologram design

The gray-scale amplitude profiles of the holographic images are calculated by the well-known Gerchberg–Saxton algorithm. Then the amplitude profiles can be discrete to multilevel (2, 4, 8). For the temporal holography display, various binary holograms with different time

constants are combined to form super-pixel holograms. The binary holograms are made of low transmission pixels and high transmission (100%) pixels. For the three-image multiplexed hologram, low transmission pixels are the perovskite without laser processing, the perovskite processed by 0.030 and 0.053 J cm⁻² laser fluence, respectively. While for the two-image multiplexed hologram, low transmission pixels are the perovskite without laser processing and the perovskite processed by 0.053 J cm⁻² laser fluence.

As for the temporally multiplexed holograms, a multiobjective gradient optimization scheme is employed to design the initial amplitude profile of the hologram, as shown in Fig. 4e. The amplitude profiles of the hologram at times T_1 , T_2 , and T_3 are determined by the experimentally measured transmission data. Fast Fourier transformation (FFT) for all the images at different times are performed and the calculated images are compared with target images by using the MSE. The total errors of the calculated three images against the target images are minimized by the gradient decent optimization, in which the gradient is the derivative of the total error with regard to all amplitude values.

Temporally programmable neural network design

The pixels of holographic layers can be considered as artificial neurons that receive, modulate, and transmit a light field. The output optical field of each neuron can be calculated by the product of the input field and the transmission coefficients of each neuron. The connections between the adjacent holographic layers are determined by the optical diffraction following the Rayleigh–Sommerfeld equation. Based on this, for the l th layer of the network, one can write the output function (n_i^l) of the i th neuron located at (x_i, y_i, z_i) as

$$n_i^l(x, y, z) = w_i^l(x, y, z) t_i^l(x_i, y_i, z_i, T) m_i^l(x_i, y_i, z_i) \quad (1)$$

where $w_i^l(x, y, z) = \frac{(z-z_i)}{r^2} (\frac{1}{2nr} + \frac{j}{\lambda}) \exp(\frac{j2\pi r}{\lambda})$ is the optical diffraction mode of the i th pixel at the l th layer according to the Rayleigh–Sommerfeld equation. λ is the operation wavelength, $r = \sqrt{(x-x_i)^2 + (y-y_i)^2 + (z-z_i)^2}$ and $j = \sqrt{-1}$. $t_i^l(x_i, y_i, z_i, T)$ is the transmission coefficient of the neurons. In our temporal neural network, the transmission coefficients $t_i^l(x_i, y_i, z_i, T)$ are spatio-temporal functions. $m_i^l(x_i, y_i, z_i) = \sum_k n_k^{l-1}(x_i, y_i, z_i)$ is the input wave to i th neuron of layer l .

To realize the time-changing functions of the neural network, the holographic layers are optimized based on the multiobjective gradient descent algorithm as shown in Supplementary Fig. 12, similar to the previous temporal holography optimization method. The holographic layers are optimized to map the input digit images at time T_1 and the input digit and fashion product images at time T_2 to the target detector region. The wave propagation between the two layers is implemented using the angular spectrum method. The optimization of the holographic layer is implemented by the TensorFlow (Google Inc.) framework. In the training process, a total cross-entropy loss function defined as the difference between the calculated output intensity distribution and the target output intensity distribution at T_1 and T_2 was used. The initial transmission coefficient of each neuron is a learnable parameter that can be iteratively adjusted by the stochastic gradient descent algorithm, Adam, to back-propagate the errors.

Direct laser writing

A fs-pulsed laser beam with a wavelength of 800 nm (Coherent, repetition rate: 80 MHz and pulse width: 100 fs) was focused on the perovskite thin film by an objective lens with a numerical aperture of 0.65. The average laser fluence was adjusted by a quarter waveplate and a linear polarizer. Wide field illumination by a red LED in the

transmission mode was added to image the sample. The dot arrays, square patterns, optical gratings, and holographic patterns were achieved by laterally translating the 3D translation stage across the focal plane and one mechanical shutter. In hologram and holographic neural network fabrication, relatively large pixels are fabricated by the line scanning method, and thus the unit pixel contains a few nanoscale lines. To construct the two-layer holographic neural networks, the perovskite thin films are, respectively, spin-coated on the two sides of a glass slide and the in-plane pixel alignment of the two layers is controlled by a nanopositioning stage with nanometer repeatability and resolution during the fabrication. Such high precision control ensures the mismatch of the two layers is far smaller than the pixel size, within which the performance of the neural network keeps very well (Supplementary Fig. 15).

Optical measurement

The optical images of perovskite thin films after laser processing were captured with an optical microscopy system (Olympus, BX53) composed of a high-definition CCD camera (DP28-CU). The temporal transmission spectra were measured using the same microscope system equipped with a spectrometer. The measurement was performed with the sample directly exposed to the air with a constant condition of 30% humidity and 25 °C. The holographic images were recorded using a home-made optical setup. The beams were generated by a semiconductor laser with a wavelength of 515 nm. The beam sequentially passes through a spatial filtering 4f system and is focused on the sample by a lens. The holographic images were collected and projected onto a CCD camera by an objective lens and a convex lens. The temporal holographic images were measured at the expected time point when the corresponding images appeared. In the measurement of the holographic neural network, the spatial light modulator was employed to encode the input images which are focused on the input plane by a 4f system. The images propagate through the sample and the output optical field was collected by a CCD. The positions of the sample and the CCD were controlled by two translation stages with micrometer resolution.

Data availability

All data needed to evaluate the conclusions in the paper are presented in the paper and/or the Supplementary Information.

References

1. Tay, S. et al. An updatable holographic three-dimensional display. *Nature* **451**, 694–698 (2008).
2. Heanue, J. F., Bashaw, M. C. & Hesselink, L. Volume holographic storage and retrieval of digital data. *Science* **265**, 749–752 (1994).
3. Qu, G. et al. Reprogrammable meta-hologram for optical encryption. *Nat. Commun.* **11**, 5484 (2020).
4. Grier, D. G. A revolution in optical manipulation. *Nature* **424**, 810–816 (2003).
5. Psaltis, D., Brady, D., Gu, X.-G. & Lin, S. Holography in artificial neural networks. *Nature* **343**, 325–330 (1990).
6. Lin, X. et al. All-optical machine learning using diffractive deep neural networks. *Science* **361**, 1004–1008 (2018).
7. Xiao, Q. et al. Broadband digital coding metasurface holography. *J. Appl. Phys.* **130** 235103 (2021).
8. Larouche, S., Tsai, Y.-J., Tyler, T., Jokerst, N. M. & Smith, D. R. Infrared metamaterial phase holograms. *Nat. Mater.* **11**, 450–454 (2012).
9. Zheng, G. et al. Metasurface holograms reaching 80% efficiency. *Nat. Nanotechnol.* **10**, 308 (2015).
10. Li, X. et al. Multicolor 3D meta-holography by broadband plasmonic modulation. *Sci. Adv.* **2**, e1601102 (2016).
11. Li, L. et al. Electromagnetic reprogrammable coding-metasurface holograms. *Nat. Commun.* **8**, 197 (2017).
12. Malek, S. C., Ee, H.-S. & Agarwal, R. Strain multiplexed metasurface holograms on a stretchable substrate. *Nano Lett.* **17**, 3641–3645 (2017).
13. Zhou, H. et al. Switchable active phase modulation and holography encryption based on hybrid metasurfaces. *Nanophotonics* **9**, 905–912 (2020).
14. Ko, B. et al. Tunable metasurfaces via the humidity responsive swelling of single-step imprinted polyvinyl alcohol nanostructures. *Nat. Commun.* **13**, 6256 (2022).
15. Li, J. et al. Addressable metasurfaces for dynamic holography and optical information encryption. *Sci. Adv.* **4**, eaar6768 (2018).
16. Kaissner, R. et al. Electrochemically controlled metasurfaces with high-contrast switching at visible frequencies. *Sci. Adv.* **7**, eabd9450 (2021).
17. Gan, Z., Cao, Y., Evans, R. A. & Gu, M. Three-dimensional deep sub-diffraction optical beam lithography with 9 nm feature size. *Nat. Commun.* **4**, 2061 (2013).
18. Ródenas, A. et al. Three-dimensional femtosecond laser nanolithography of crystals. *Nat. Photonics* **13**, 105–109 (2019).
19. Xu, X. et al. Femtosecond laser writing of lithium niobate ferroelectric nanodomains. *Nature* **609**, 496–501 (2022).
20. Zhang, Y. et al. Full-visible multifunctional aluminium metasurfaces by in situ anisotropic thermoplasmonic laser printing. *Nanoscale Horiz.* **4**, 601–609 (2019).
21. Li, X. et al. Athermally photoreduced graphene oxides for three-dimensional holographic images. *Nat. Commun.* **6**, 6984 (2015).
22. Yue, Z., Xue, G., Liu, J., Wang, Y. & Gu, M. Nanometric holograms based on a topological insulator material. *Nat. Commun.* **8**, 15354 (2017).
23. Wang, Y. et al. Atomically thin noble metal dichalcogenides for phase-regulated meta-optics. *Nano Lett.* **20**, 7811–7818 (2020).
24. Chen, P. et al. Laser nanoprinting of 3D nonlinear holograms beyond 25000 pixels-per-inch for inter-wavelength-band information processing. *Nat. Commun.* **14**, 5523 (2023).
25. Zhang, W. et al. Structural multi-colour invisible inks with submicron 4D printing of shape memory polymers. *Nat. Commun.* **12**, 112 (2021).
26. Zhang, W. et al. Stiff shape memory polymers for high-resolution reconfigurable nanophotonics. *Nano Lett.* **22**, 8917–8924 (2022).
27. Correa-Baena, J.-P. et al. Promises and challenges of perovskite solar cells. *Science* **358**, 739–744 (2017).
28. Green, M. A., Ho-Baillie, A. & Snaith, H. J. The emergence of perovskite solar cells. *Nat. Photonics* **8**, 506–514 (2014).
29. Huang, C. et al. Ultrafast control of vortex microlasers. *Science* **367**, 1018–1021 (2020).
30. Zhang, C. et al. Dynamic perovskite metasurfaces: lead halide perovskite-based dynamic metasurfaces. *Laser Photonics Rev.* **13**, 1970030 (2019).
31. Huang, X. et al. Reversible 3D laser printing of perovskite quantum dots inside a transparent medium. *Nat. Photonics* **14**, 82–88 (2020).
32. Sun, K. et al. Three-dimensional direct lithography of stable perovskite nanocrystals in glass. *Science* **375**, 307–310 (2022).
33. Fan, Y. et al. Resonance-enhanced three-photon luminescence via lead halide perovskite metasurfaces for optical encoding. *Nat. Commun.* **10**, 2085 (2019).
34. Gao, Y. et al. Lead halide perovskite nanostructures for dynamic color display. *ACS Nano* **12**, 8847–8854 (2018).
35. Dučinskas, A. et al. Unravelling the behavior of Dion-Jacobson layered hybrid perovskites in humid environments. *ACS Energy Lett.* **6**, 337–344 (2021).
36. Du, K.-Z. et al. Two-dimensional lead(II) halide-based hybrid perovskites templated by acene alkylamines: crystal structures, optical properties, and piezoelectricity. *Inorg. Chem.* **56**, 9291–9302 (2017).
37. Leng, K. et al. Molecularly thin two-dimensional hybrid perovskites with tunable optoelectronic properties due to reversible surface relaxation. *Nat. Mater.* **17**, 908–914 (2018).

38. Leng, K., Fu, W., Liu, Y., Chhowalla, M. & Loh, K. P. From bulk to molecularly thin hybrid perovskites. *Nat. Rev. Mater.* **5**, 482–500 (2020).
39. Giri, A. et al. Ultralow thermal conductivity of two-dimensional metal halide perovskites. *Nano Lett.* **20**, 3331–3337 (2020).
40. Gu, M., Fang, X., Ren, H. & Goi, E. Optically digitalized holography: a perspective for all-optical machine learning. *Engineering* **5**, 363–365 (2019).
41. Zhang, Q., Yu, H., Barbiero, M., Wang, B. & Gu, M. Artificial neural networks enabled by nanophotonics. *Light Sci. Appl.* **8**, 42 (2019).
42. Goi, E. et al. Nanoprinted high-neuron-density optical linear perceptrons performing near-infrared inference on a CMOS chip. *Light Sci. Appl.* **10**, 40 (2021).
43. Goi, E., Schoenhardt, S. & Gu, M. Direct retrieval of Zernike-based pupil functions using integrated diffractive deep neural networks. *Nat. Commun.* **13**, 7531 (2022).
44. Chen, Y. et al. All-analog photoelectronic chip for high-speed vision tasks. *Nature* **623**, 48–57 (2023).
45. Zhou, T. et al. Large-scale neuromorphic optoelectronic computing with a reconfigurable diffractive processing unit. *Nat. Photonics* **15**, 367–373 (2021).
46. Liu, C. et al. A programmable diffractive deep neural network based on a digital-coding metasurface array. *Nat. Electron.* **5**, 113–122 (2022).

Acknowledgements

We thank X. Fang and J. Wei for inversely optimizing the temporal holography, X. Li for fluorescence measurement, and Q. Zhang for discussion. The authors acknowledge funding support from the Shanghai Municipal Science and Technology Major Project, Science and Technology Commission of Shanghai Municipality (No. 21DZ1100500 (M.G.)), Shanghai Frontiers Science Center Program (2021–2025 No. 20 (M.G.)). Y.Z. acknowledges the support from the Program for Professor of Special Appointment (Eastern Scholar) at Shanghai Institutions of Higher Learning, National Natural Science Foundation of China (No. 62175154 (Y.Z.)), and Shanghai Science and Technology Program (21ZR1445500 (Y.Z.)).

Author contributions

M.G. and Y.Z. conceived the concept and supervised the research. Y.Z. discovered the hydration control and proposed the mechanism. Y.Z. and S.Z. conducted the hologram and holographic neural network calculations and characterizations, material characterizations, and direct laser

writing. J.H. helped synthesize the perovskite materials and perform the XRD/XPS characterizations. Y.Z. wrote the manuscript. All authors participated in discussions.

Competing interests

The authors declare no competing interests.

Additional information

Supplementary information The online version contains supplementary material available at <https://doi.org/10.1038/s41467-024-51148-5>.

Correspondence and requests for materials should be addressed to Yinan Zhang or Min Gu.

Peer review information *Nature Communications* thanks Dong Wu and the other, anonymous, reviewer(s) for their contribution to the peer review of this work. A peer review file is available.

Reprints and permissions information is available at <http://www.nature.com/reprints>

Publisher's note Springer Nature remains neutral with regard to jurisdictional claims in published maps and institutional affiliations.

Open Access This article is licensed under a Creative Commons Attribution-NonCommercial-NoDerivatives 4.0 International License, which permits any non-commercial use, sharing, distribution and reproduction in any medium or format, as long as you give appropriate credit to the original author(s) and the source, provide a link to the Creative Commons licence, and indicate if you modified the licensed material. You do not have permission under this licence to share adapted material derived from this article or parts of it. The images or other third party material in this article are included in the article's Creative Commons licence, unless indicated otherwise in a credit line to the material. If material is not included in the article's Creative Commons licence and your intended use is not permitted by statutory regulation or exceeds the permitted use, you will need to obtain permission directly from the copyright holder. To view a copy of this licence, visit <http://creativecommons.org/licenses/by-nc-nd/4.0/>.

© The Author(s) 2024